

# Calculation of femtosecond pulse laser induced damage threshold for broadband antireflective microstructure arrays

Xufeng Jing,<sup>1,2\*</sup> Jianda Shao,<sup>1</sup> Junchao Zhang,<sup>1,2</sup>  
Yunxia Jin,<sup>1</sup> Hongbo He,<sup>1</sup> and Zhengxiu Fan<sup>1</sup>

<sup>1</sup> Key Laboratory of Materials for High Power Laser, Shanghai Institute of Optics and Fine Mechanics, Chinese Academy of Sciences, Shanghai 201800, PR China

<sup>2</sup> Graduate School of Chinese Academy of Sciences, Beijing 100039, PR China  
\* jingxufeng\_1984@yahoo.com.cn

**Abstract:** In order to more exactly predict femtosecond pulse laser induced damage threshold, an accurate theoretical model taking into account photoionization, avalanche ionization and decay of electrons is proposed by comparing respectively several combined ionization models with the published experimental measurements. In addition, the transmittance property and the near-field distribution of the ‘moth eye’ broadband antireflective microstructure directly patterned into the substrate material as a function of the surface structure period and groove depth are performed by a rigorous Fourier model method. It is found that the near-field distribution is strongly dependent on the periodicity of surface structure for TE polarization, but for TM wave it is insensitive to the period. What’s more, the femtosecond pulse laser damage threshold of the surface microstructure on the pulse duration taking into account the local maximum electric field enhancement was calculated using the proposed relatively accurate theoretical ionization model. For the longer incident wavelength of 1064nm, the weak linear damage threshold on the pulse duration is shown, but there is a surprising oscillation peak of breakdown threshold as a function of the pulse duration for the shorter incident wavelength of 532nm.

©2009 Optical Society of America

**OCIS:** (050. 6624) Subwavelength structures; (220. 4000) Microstructure fabrication; (310.1210) Antireflection; (140.3440) Laser-induced breakdown; (320.2250) Femtosecond phenomena.

---

## References and links

1. D. Du, X. Liu, G. Korn, J. Squier, and G. Mourou, “Laser-induced breakdown by impact ionization in SiO<sub>2</sub> with pulse widths from 7 ns to 150 fs,” *Appl. Phys. Lett.* **64**(23), 3071–3073 (1994).
2. B. C. Stuart, M. D. Feit, A. M. Rubenchik, B. W. Shore, and M. D. Perry, “Laser-induced damage in dielectrics with nanosecond to subpicosecond pulses,” *Phys. Rev. Lett.* **74**(12), 2248–2251 (1995).
3. M. Lenzner, J. Krüger, S. Sartania, Z. Cheng, Ch. Spielmann, G. Mourou, W. Kautek, and F. Krausz, “Femtosecond Optical Breakdown in Dielectrics,” *Phys. Rev. Lett.* **80**(18), 4076–4079 (1998).
4. A.-C. Tien, S. Backus, H. Kapteyn, M. Murnane, and G. Mourou, “Short-Pulse Laser Damage in Transparent Materials as a Function of Pulse Duration,” *Phys. Rev. Lett.* **82**(19), 3883–3886 (1999).
5. J. Jasapara, A. V. V. Nampoothiri, W. Rudolph, D. Ristau, and K. Starke, “Femtosecond laser pulse induced breakdown in dielectric thin films,” *Phys. Rev. B* **63**(4), 045117 (2001).
6. M. Mero, J. Liu, W. Rudolph, D. Ristau, and K. Starke, “Scaling laws of femtosecond laser pulse induced breakdown in oxide films,” *Phys. Rev. B* **71**(11), 115109 (2005).
7. Y. Kanamori, M. Sasaki, and K. Hane, “Broadband antireflection gratings fabricated upon silicon substrates,” *Opt. Lett.* **24**(20), 1422–1424 (1999).
8. D. S. Hobbs, B. D. MacLeod, and J. R. Riccobono, “Update on the development of high performance antireflecting surface relief micro-structures,” *Proc. SPIE* **6545**, 65450Y (2007).
9. W. H. Lowdermilk, and D. Milam, “Graded-index antireflection surfaces for high-power laser applications,” *Appl. Phys. Lett.* **36**(11), 891–893 (1980).
10. K. Starke, D. Ristau, H. Welling, T. V. Amotchkina, M. Trubetskov, A. A. Tikhonravov, and A. S. Chirkin, “Investigations in the nonlinear behavior of dielectrics by using ultrashort pulses,” *Proc. SPIE* **5273**, 501–514 (2004).

11. L. V. Keldysh, "Ionization in the field of a strong electromagnetic wave," *Sov. Phys. JETP* **20**, 1307–1314 (1965).
12. L. Sudrie, A. Couaillon, M. Franco, B. Lamouroux, B. Prade, S. Tzortzakis, and A. Mysyrowicz, "Femtosecond laser-induced damage and filamentary propagation in fused silica," *Phys. Rev. Lett.* **89**(18), 186601 (2002).
13. L. Yuan, Y. A. Zhao, G. Q. Shang, C. R. Wang, H. B. He, J. D. Shao, and Z. X. Fan, "Comparison of femtosecond and nanosecond laser-induced damage in HfO<sub>2</sub> single-layer film and HfO<sub>2</sub>-SiO<sub>2</sub> high reflector," *J. Opt. Soc. Am. B* **24**(3), 538–543 (2007).
14. M. Jupé, L. Jensen, A. Melninkaitis, V. Sirutkaitis, and D. Ristau, "Calculations and experimental demonstration of multi-photon absorption governing fs laser-induced damage in titania," *Opt. Express* **17**(15), 12269–12278 (2009).
15. B. C. Stuart, M. D. Feit, S. Herman, A. M. Rubenchik, B. W. Shore, and M. D. Perry, "Nanosecond-to-femtosecond laser-induced breakdown in dielectrics," *Phys. Rev. B* **53**(4), 1749–1761 (1996).
16. B. Rethfeld, "Unified model for the free-electron avalanche in laser-irradiated dielectrics," *Phys. Rev. Lett.* **92**(18), 187401 (2004).
17. A. Vaidyanathan, T. W. Walker, and A. H. Guenther, "The relative roles of avalanche multiplication and multiphoton absorption in laser-induced damage of dielectrics," *IEEE J. Quantum Electron.* **16**(1), 89–93 (1980).
18. P. N. Saeta, and B. I. Greene, "Primary relaxation processes at the band edge of SiO<sub>2</sub>," *Phys. Rev. Lett.* **70**(23), 3588–3591 (1993).
19. M. Li, S. Menon, J. P. Nibarger, and G. N. Gibson, "Ultrafast Electron Dynamics in Femtosecond Optical Breakdown of Dielectrics," *Phys. Rev. Lett.* **82**(11), 2394–2397 (1999).
20. T. Q. Jia, Z. Z. Xu, R. X. Li, D. H. Feng, X. X. Li, C. F. Cheng, H. Y. Sun, N. S. Xu, and H. Z. Wang, "Mechanisms in fs-laser ablation in fused silica," *J. Appl. Phys.* **95**(9), 5166–5171 (2004).
21. L. F. Li, "New formulation of the Fourier modal method for crossed surface-relief gratings," *J. Opt. Soc. Am. A* **14**(10), 2758–2767 (1997).
22. S. J. Liu, Z. C. Shen, W. J. Kong, J. Shen, Z. X. Deng, Y. A. Zhao, J. D. Shao, and Z. X. Fan, "Optimization of near-field optical field of multi-layer dielectric gratings for pulse compressor," *Opt. Commun.* **267**(1), 50–57 (2006).
23. J. Y. Ma, S. J. Liu, Y. X. Jin, C. Xu, J. D. Shao, and Z. X. Fan, "Novel method for design of surface relief guided-mode resonant gratings at normal incidence," *Opt. Commun.* **281**(12), 3295–3300 (2008).
24. L. F. Li, "Note on the *S*-matrix propagation algorithm," *J. Opt. Soc. Am. A* **20**(4), 655–660 (2003).
25. D. M. Simanovskii, H. A. Schwettman, H. Lee, and A. J. Welch, "Midinfrared optical breakdown in transparent dielectrics," *Phys. Rev. Lett.* **91**(10), 107601 (2003).
26. D. Du, X. Liu, and G. Mourou, "Reduction of multi-photon ionization in dielectrics due to collisions," *Appl. Phys. B* **63**, 617–621 (1996).

## 1. Introduction

With the development of high-power laser system, the power output and operational lifetime for high-intensity lasers depend critically on enhancing laser induced damage threshold (LIDT) and eliminating reflection from the surface of their numerous optical components. Thus, it is important to investigate the laser damage characteristic of transparent bulk dielectrics and transmitting optical components in femtosecond pulse region. For the laser pulse duration  $\tau_p < 10$  ps, it is known that the LIDT on the pulse width exhibits a significant deviation from the scaling law  $\tau_p^{1/2}$  characterizing the breakdown threshold for  $\tau_p > 10$  ps and the highly deterministic and intrinsic damage performance. Nevertheless, a contradiction in the experimental results was observed. Du *et al.* [1] reported that the LIDT demonstrates the increasing tendency as the pulse width decreases. Later, Stuart *et al.* [2], Lenzner *et al.* [3] and Tien *et al.* [4] confirmed the departure from the scaling law, but their measurements under approximately similar conditions displayed a decreasing threshold associated with a gradual transition from the long-pulse to ultra-short duration regime. Both behaviors were explained via different theoretical models on the basis of the combined effect of electron impact and multiphoton ionization processes. However, these theoretical models only yield partially satisfactory agreement with experimental observations. Hence, laser damage mechanism on ultra-short time scales remains an active area of research.

Recently, Jasapara *et al.* [5] and Mero *et al.* [6] focused on the investigation of the damage of dielectric thin films in subpicosecond pulse regime taking into account local intensity enhancement due to interference effects in the coatings. Therefore, to our knowledge, recent work mostly concentrated on the damage of bulk dielectric materials and optical thin films in ultra-short pulse range. Then it is uncommon to quantitatively investigate the breakdown property of a broadband antireflective microstructure (BAM) in femtosecond pulse duration region in literatures. With the development of microfabrication technologies, it is well known

that the ‘moth eye’ BAM has attracted more and more attention not only in the performance of antireflection for wide range of spectrum and wide incident angle range [7] but also in high LIDT [8,9]. And the BAM patterned directly into a bulk substrate is expected to be used in high-power laser systems as an advanced laser-transmitting optical element.

In this paper, a theoretical model allowing for photoionization (PI), avalanche ionization (AI), and electron diffusion and recombination process for more accurately predicting the LIDT was proposed by comparing respectively several kinds of theoretical models applied commonly in literatures with the reported experimental data. Furthermore, due to dielectric breakdown exhibiting a strong dependence on the electric field intensity in femtosecond range, the near-field distribution of BAM on the basis of the high transmittance analysis was simulated numerically by a rigorous Fourier model method. Afterwards, the femtosecond LIDT of the BAM taking into account maximum local electric field enhancement was calculated employing the proposed theoretical model, and the scaling law of threshold fluences as a function of femtosecond pulse duration was exhibited.

## 2. Theory of ultra-short pulse laser induced damage

For intense ultra-short pulses, the duration is significantly shorter than the time scale for electron energy transfer to the lattice. As a result, the heat conduction effect caused by nanosecond or subpicosecond pulses can be negligible for dielectrics breakdown. Although the actual processes leading to femtosecond laser-pulse-induced dielectric breakdown and ablation are complex and still under investigation, it is commonly accepted that the damage of materials can be explained by the nonlinear excitation of electrons from the valence band (VB) to the conduction band (CB) via processes such as AI and PI including multiphoton ionization (MPI) and tunneling ionization (TI), in which PI initiate the seed electrons in the CB from the VB and the electrons are then heated rapidly by the pulse resulting in further collision ionization. When the electron density (ED) in the CB reaches a critical electron density (CED) of  $n_{cr}$  considered generally as damage criterion, the material absorbs strongly through the process of inverse bremsstrahlung resulting in ablation and permanent structural changes. Usually the CED is assumed to reach when the respective plasma waves are resonant with the incident laser wavelength, which is represented by [10]

$$n_{cr} = \frac{\epsilon_0 m_e^* \omega^2}{e^2}, \quad (1)$$

where  $e$  is the electron charge,  $\epsilon_0$  is the permittivity of free space, and  $m_e^*$  and  $\omega$  denote the effective electron mass and the incident laser frequency, respectively.

A rate equation to determine the evolution of the free ED  $n_e(t)$  in a dielectric medium exposed to laser pulses below 10ps was written as

$$\frac{\partial n_e(t)}{\partial t} = W_{PI}(I(t)) + W_{Av}(I(t)) \cdot n_e(t) - W_{rel}(n(t), t), \quad (2)$$

where  $W_{PI}(I(t))$  and  $W_{Av}(I(t))$  are the PI rate and AI rate, respectively, which are dependent on the incident intensity, and  $W_{rel}(n(t), t)$  is the plasma energy decay term associated with the diffusion and recombination of electrons.

### 2.1 Photoionization

For the PI rate  $W_{PI}(I(t))$  in Eq. (2), Keldysh’s PI theory is most commonly used to calculate the excitation rate of electrons, which is shown as [11]

$$W_{PI}(I(t)) = \frac{2\omega}{9\pi} \left( \frac{\omega m_e^*}{\sqrt{\gamma_1} \hbar} \right)^{3/2} Q(\gamma, x) \exp \left\{ -\pi \langle x+1 \rangle \frac{K(\gamma_1) - E(\gamma_1)}{E(\gamma_2)} \right\}, \quad (3)$$

where the adiabaticity parameter (Keldysh parameter) for solid is  $\gamma = \omega \sqrt{m_e^* E_g} / eE$ ,  $m_e^* = \frac{m_e m_h}{m_e + m_h}$  denotes the reduced mass of the electron and the hole,  $E$  is the electric field amplitude of the radiation,  $E_g$  is intrinsic material gap, and  $\gamma_1 = \gamma^2 / (1 + \gamma^2)$  and  $\gamma_2 = 1 / (1 + \gamma^2)$  in addition to

$$Q(\gamma, x) = \sqrt{\frac{\pi}{2K(\gamma_2)}} \times \sum_{n=0}^{\infty} \exp \left\{ -n\pi \frac{K(\gamma_2) - E(\gamma_2)}{E(\gamma_1)} \right\} \Phi \left\{ \frac{\pi}{2} \sqrt{\frac{(2\langle x+1 \rangle - 2x + n)}{K(\gamma_2)E(\gamma_2)}} \right\},$$

$$x = \frac{2}{\pi} \frac{E_g}{\hbar\omega} \frac{\sqrt{1+\gamma^2}}{\gamma} E \left( \frac{1}{1+\gamma^2} \right), \quad \Phi(z) = \int_0^z \exp(y^2 - z^2) dy,$$

where  $K$  and  $E$  represent the complete elliptic integral of the first and second kinds, respectively,  $\langle \dots \rangle$  denotes the integer part and  $\Phi$  describes the Dawson function.

In the case of high laser frequencies and low electric fields ( $\gamma \gg 1$ ), the PI rate describes the probability for MPI, and the ionization rate can be approximately by

$$W_{multi} = \frac{2\omega}{9\pi} \left( \frac{m_e^* \omega}{\hbar} \right)^{3/2} \Phi \left( \sqrt{2\langle E_g' / \hbar\omega + 1 \rangle - 2E_g' / \hbar\omega} \right) \times \exp \left\{ 2\langle E_g' / \hbar\omega + 1 \rangle \left( 1 - \frac{1}{4\gamma^2} \right) \right\} \left( \frac{1}{16\gamma^2} \right)^{\langle E_g' / \hbar\omega + 1 \rangle}, \quad (4)$$

where  $E_g' = E_g [1 + (1/2\gamma^2)]$  represents the effective band gap energy in the radiation field. For high electric fields and low laser frequencies ( $\gamma \ll 1$ ), the opposite case of photon-induced TI is represented. Keldysh derived an approximation for the ionization rate as

$$W_{tunnel} = \frac{2\omega}{9\pi^2 \hbar} \left( \frac{m_e^* E_g}{\hbar^2} \right)^{3/2} \left( \frac{\hbar\omega}{E_g \gamma} \right)^{5/2} \exp \left\{ -\frac{\pi}{2} \frac{E_g \gamma}{\hbar\omega} \left( 1 - \frac{\gamma^2}{8} \right) \right\}. \quad (5)$$

In other words, Keldysh's PI rate asymptotically approaches MPI and TI at the two extreme limits of the field as might be expected from an analogy with the atomic case.

A general analytical solution of Eq. (3) is not available, and the Keldysh ionization rate has to be determined numerically. Moreover, it is commonly known that the precise value of the effective electron mass (EEM)  $m_e^*$  in materials for calculating PI rate and AI rate is **not available in literatures**. And it is worth mentioned that the EEM is strongly dependent on the material properties and categories. Usually,  $m_e^* = 0.635m_e$  is a measured value which is accepted to be accurate for quartz [12], and  $m_e$  is the real electron mass. In addition, the  $0.5m_e$  of the EEM is often used in theoretical calculations on fused silica [13], and the  $0.3m_e$  is fitted from experimental data for titania single layers [14].

Thus, PI rate as a function of electric field with the several commonly applied values of the EEM mentioned for the both band gap of 9eV and 3.6eV, respectively, was calculated in Fig. 1. It can be seen that the effect of the varying EEM to PI rate is not significant in the limit of MPI and TI regimes for the both band gaps. And for smaller gap (3.6eV) the influence of

the different EEM values is slight for all the intensity range. But the variation of  $m_e^*$  by factor of around 2.1 can vary maximally the PI rate by about 2 orders of magnitude in intermediate intensity regime for the larger band gap (9eV). In our calculation,  $m_e^* = 0.635m_e$  is used to estimate PI rate. Besides, the PI rate  $W_{PI}$  as a function of the laser intensity for the band gap  $E_g = 9$  eV is shown in Fig. 2. It can be seen that the  $W_{PI}$  approaches asymptotically Keldysh's MPI rate and TI rate at the extreme limits of weak and strong fields. In addition, it is worth noting that in the MPI regime the ionization rate  $P(I)_{MPI} = \sigma_k I^k$ , where  $\sigma_k$  is the MPI absorption coefficient for absorption of  $k$  photons, was used by Stuart *et al.* in their derived rate equation [15], but it was illustrated that this used MPI rate is only valid for the laser intensity lower than around  $4 \text{ TW/cm}^2$  [12].

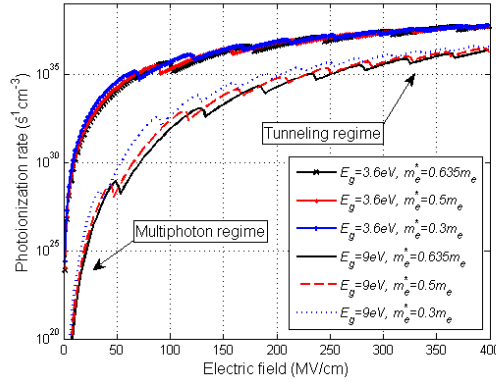


Fig. 1. Typical PI rate with respect to electric field with the effective electron masses of  $0.635m_e$ ,  $0.5m_e$  and  $0.3m_e$ , respectively, for the both material gap of 9eV and 3.6eV.

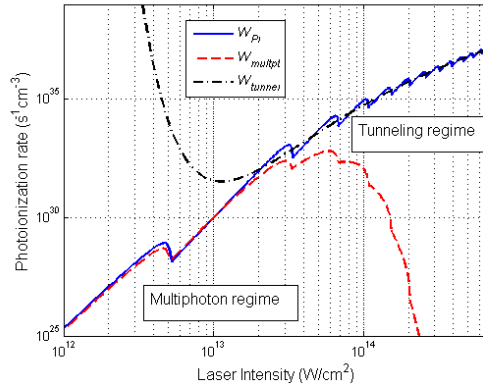


Fig. 2. PI rate on the laser intensity with gap  $E_g = 9$  eV from Keldysh's theory, the incident wavelength is  $\lambda = 800 \text{ nm}$ , and the multiphoton and tunnel limits are also shown.

## 2.2 Avalanche ionization

When the dielectric is radiated by intense laser, an electron in the CB absorbs laser photons, sequentially moving to higher energy states with the conversation of **energy** and **momentum**. After the sequential absorption of  $n$  photons, where  $n$  is the smallest number which satisfies

the relation  $n\hbar\omega \geq E_g$ , the electron's energy exceeds the CB minimum by more than the band-gap energy. Then the electron can collisionally ionize another electron from the VB. The result of the AI is two electrons near the CB minimum, each of which can absorb successively photons and subsequently impact ionize additional VB electrons. In addition, AI requires some seed electrons in the CB, and it is assumed that these initial electrons are provided directly by PI in femtosecond pulse range.

In general, it is known that several kinds of commonly applied AI theoretical models only yield partially satisfactory agreement with experimental observations in literatures. In order to quantitatively demonstrate the distinction of AI rate contributing to the CB electron density as a function of electric field strength among the reported AI models, the several AI theoretical models frequently used in literatures for predicting the AI rate are shown in the following sections.

### 2.2.1 Stuart model [2,15]

Recently, Stuart *et al.* derived a model of AI in which the rate depends linearly on the laser intensity as

$$W_{Av-Stuart} = \alpha \cdot I(t), \quad (6)$$

where  $I(t) = (1/2)cn_0\varepsilon_0|E(t)|^2$ , and the avalanche coefficient  $\alpha \approx 0.01 \text{ cm}^2\text{ps}^{-1}/\text{GW}$  was found by numerically solving a Fokker-Planck equation describing the electron dynamics in the CB. Although this model has been applied successfully to predict the pulse duration dependence of the breakdown threshold fluence in the ultra-short pulse domain [3], some associated researchers consider that the applicability of this avalanche rate linearly scaled with laser intensity is doubtful [16]. The linear relationship between the AI rate and the laser intensity is the consequence of two major assumptions violated in a strong electric field [4]. But it is believed that the Stuart avalanche model is valid to apply in relatively low field strength.

### 2.2.2 Sparks model [13,17]

A simplified model of avalanche multiplication rate  $W_{Av\_Sparks}$  assuming constant collision frequencies and energy loss was outlined by Sparks [17]. This model assumes energy gain of a conduction electron from an alternating electric field, once the conduction electron has attained the energy equal to the band-gap energy, it can excite a valence electron across the band-gap, and this process repeats itself. The AI rate is shown as

$$W_{Av\_Sparks} = \frac{0.693e^2E^2\tau_K}{m_e^*E_g(1+\omega^2\tau_K^2)} - \frac{0.693\hbar\omega_p}{E_g\tau_L}, \quad (7)$$

where  $\tau_K = 1.36 \times 10^{-15} \text{ s}$  is the electron-phonon relaxation time when only large-angle scattering is considered,  $\tau_L = 8.77 \times 10^{-16} \text{ s}$  is the relaxation time when both large- and small-angle scatterings are considered,  $\omega_p$  is the average phonon frequency, and  $\hbar\omega_p = 0.025 \text{ eV}$ .

### 2.2.3 Thornber model [1,4]

The Thornber AI model is based on the excursion and acceleration of the CB electrons in a dc electric field. When the CB electron gains the enough energy, it can excite a VB electron. This empirical model is applicable for all electric field strengths, which is essential when comparing to the published experimental data [1]. The expression of AI rate is represented by

$$W_{Av\_Thornber} = \frac{\nu_s e E}{E_g} \exp\left\{-\frac{E_l}{E(1 + E/E_{phonon}) + E_{kT}}\right\}, \quad (8)$$

where  $v_s$  is the saturation drift velocity ( $\approx 2 \times 10^7$  cm/s),  $E_I$  (30 MV/cm),  $E_{\text{phonon}}$  (3.2 MV/cm), and  $E_{kT}$  (0.01 MV/cm)  $\equiv E_I kT / E_g$  are the fields for carriers to overcome the decelerating effects of ionization scattering, optical phonon scattering, and thermal scattering in one mean free path, respectively.

#### 2.2.4 Drude model [10,14]

The ionization rate  $W_{\text{Av\_Drude}}$  of Drude model can be deduced in first order by the heating of free electrons, which is associated with the absorption coefficient obtained by separating the imaginary part of the complex refractive index induced by plasma formation in dielectrics. If electrons can attain a kinetic energy equal to the band-gap during the typical **collision time** which is reciprocal to the electron density, secondary electrons are produced with the following AI rate:

$$W_{\text{Av\_Drude}} = \frac{\sigma}{E_g} \cdot I(t), \quad (9)$$

$$\sigma = \frac{e^2}{c\epsilon_0 n_e^*} \cdot \frac{\tau_c}{1 + \omega^2 \tau_c^2}, \quad \tau_c = \frac{16\pi\epsilon_0^2 \sqrt{m_e^*} (0.1E_g)^3}{\sqrt{2}e^4 n(t)},$$

where  $\sigma$  is the absorption cross section, and  $\tau_c$  is the resulting collision time which is reciprocal to the electron density.

On the basis of above description of the several ionization mechanism models, the AI rate as a function the incident electric field is performed for Stuart model, Thornber model and Sparks model, respectively, in Fig. 3. The ionization rate of Drude model is not included in Fig. 3 due to the collision time  $\tau_c$  in Eq. (9) is related to the ED  $n(t)$ .

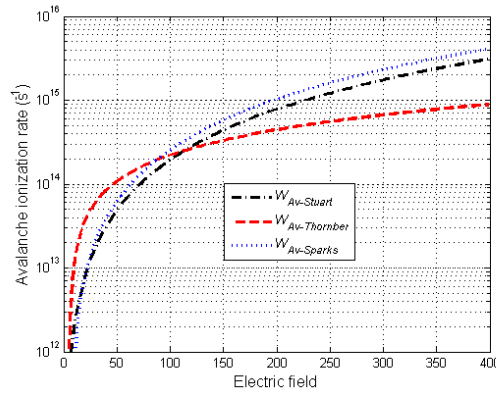


Fig. 3. AI rate as a function of the incident electric field for the AI models of Stuart, Thornber and Sparks, respectively.

#### 2.3 Decay of electrons

In contrast to the process of the increasing electrons resulted from the PI and AI in CB, the decay behavior of the electrons is also important to the damage process of materials. The most prominent decay process is known as the generation of self-trapped excitation with which the CB electrons move back to the VB depending on the relevant time scale. Some researchers believed that in the ultra-short pulse duration region the loss term due to electron diffusion and recombination of self-trapped excitation can be neglected to calculate the evolution of ED in the CB [2,15]. But the fast recombination process with a relaxation time  $\tau_r$  between 150



and 250 fs for dielectrics was found [18]. Moreover, Li *et al.* have indicated that the plasma energy in dielectrics experiences ultra-fast decay which lasts only ~100 fs and does not follow an exponential decay curve by using pump-probe double pulse measurements [19]. Therefore, a decay term **must be** included in the ED rate equation of Eq. (2). In our calculation, the relaxation time  $\tau_r = 100$  fs was applied and the recombination rate was approximated by

$$W_{rel} = \frac{n(t)}{\tau_r}. \quad (10)$$

According to the PI rate, AI rate and the diffusion and recombination of CB electrons described, respectively, in former sections, Fig. 4 shows the total evolution of ED in the CB calculated by the rate equation of Eq. (2) for the four combining ionization models. The calculation parameters are shown in the annotation of Fig. 4. Assuming a Gaussian temporal pulse shape  $I = I_0 \exp[-4 \ln(2)(t/\tau_p)^2]$  with  $I_0 = 23.85$  TW/cm<sup>2</sup>, the fluence is  $\varphi = (\pi/\ln 2)^{1/2} I_0 \tau_p / 2 \approx 2.54$  J/cm<sup>2</sup>. It can be seen in Fig. 4 that the total evolution of the ED calculated by the combining the Keldysh's PI with the AI model of Drude reaches exactly to the demonstrated CED  $n_{cr}$  as the damage criterion with the selected fluence of 2.54 J/cm<sup>2</sup>. In other words, the fluence of 2.54 J/cm<sup>2</sup> is the LIDT predicted by this combining ionization model. But the total evolution of the ED estimated by the combining the Keldysh's PI with the other AI models much surpasses the CED in Fig. 4. Then, it can be derived that the LIDT calculated by these combining ionization models is much lower than the fluence of 2.54 J/cm<sup>2</sup>. Besides, it is known that a typical surface damage threshold of  $\varphi \approx 2.8$  J/cm<sup>2</sup> was measured, which the experimental parameters are the similar with our calculation [3,4,10]. Therefore, the LIDT calculated by combining the Keldysh's PI and Drude AI model in Eq. (2) **using the CED  $n_{cr}$  as the damage criterion** approaches mostly the experimental result. The difference between our theoretical result and the published experimental data can be explained to arise from experimental conditions and parameters uncertainty of the applied model. For the experimental conditions, the different methods of measurement to define the damage could bring about the discrepancy of the detected LIDT. For instance, it is usually used to define the damage threshold by **any visible permanent modification** to the sample with the indirect metrology equipments such as Nomarski microscope and SEM, and plasma emission detected by CCD from the focal region in the sample. In addition, to **measure the variation of reflectivity or transmittivity** of the sample using the pump-probe method is also utilized commonly to determine the LIDT. Furthermore, the incubation effect of a series of subthreshold pulses is an important factor to determine damage threshold. For the uncertainty of the model itself combining the PI rate and the Drude AI rate in addition to the decay of the electrons, the imprecise parameters applied such as the effective electron mass, the typical collision time and the relaxation time of the CB electrons could lead to the inaccurate result of the calculated LIDT. Besides, the certain constants included in model also need to be fitted or approximated, and the calculated AI rate based on Drude model strongly overestimates the ionization rate obtained by the multiple rate equation which was proposed by Rethfeld considering the detailed kinetic approaches [16]. Moreover, Jia *et al.* [20] reported that the calculated LIDT taking the **deposited energy density** as the damage and ablation criterion for fused silica, which was in agreement well with their experimental results, was larger than that taking the CED as the breakdown criterion. Although many uncertainties concerning the calculated result and the publish experimental data, the LIDT determined by combining the Keldysh's PI with Drude AI model in addition to the decay term in Eq. (2) is in agreement reasonable with the experimental measurements.

Moreover, it can be obtained from the ED evolution produced by only Keldysh's PI in Fig. 4 that the PI excite the initial ED to provide the seed electrons for the subsequent AI, and the CED dominating damage threshold is reached by latter AI. Subsequently, we would calculate



the LIDT of BAM with the proposed more accurate combining ionization model in femtosecond pulse range.

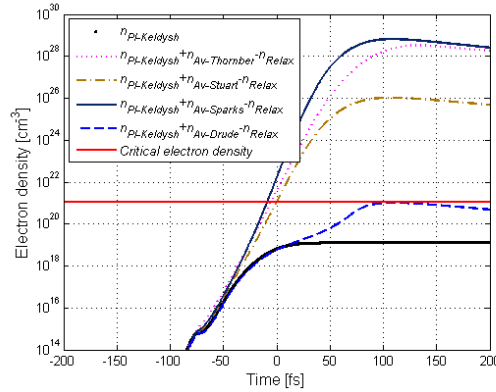


Fig. 4. Total evolution of free electron density based on the Eq. (2) for the combining Keldysh's PI with the AI models of Thornber, Stuart, Sparks and Drude, respectively. And the evolution of ED produced only by Keldysh's PI is also shown for reference. A Gaussian pulse of peak intensity  $I_0 = 23.85 \text{ TW/cm}^2$  with the pulse duration of 100fs and the incident wavelength of 800nm is selected to produce the ED. The material parameters of the refractive index  $n_0 = 1.46$ , band gap  $E_g = 9\text{eV}$ , the reduced electron mass  $m_e^* = 0.635m_e$  and the relaxation time  $\tau_r = 100\text{fs}$  are applied to calculate ED evolution. Besides, the CED

$$n_{cr} = (\epsilon_0 m_e^* \omega^2) / e^2 = 1.1 \times 10^{21} \text{ cm}^{-3} \text{ is demonstrated as the damage criterion.}$$

### 3. Optical performance of the broadband antireflective microstructure arrays

Figure 5 shows the schematic diagram of BAM arrays.  $\Lambda$  and  $d$  denote the periodicity and groove depth, respectively.  $n_0$  and  $n_g$  are the refractive indices of the surrounding medium and substrate material, respectively. Here, the value of  $n_0$  is equal to 1.0, and the value of  $n_g$  is taken from the refractive index of 1.46. The microstructure arrays analyzed are directly patterned into the substrate medium, and the linear absorption loss and dispersion effect in the substrate material are ignored. In addition, we specify the orientation of the electric field  $\mathbf{E}$  with respect to the profile vector  $\mathbf{K}$ , which depend on electric field  $\mathbf{E}$  of incident wave parallel to the profile vector  $\mathbf{K}$  (TM polarization) or perpendicular to the profile vector  $\mathbf{K}$  (TE polarization).

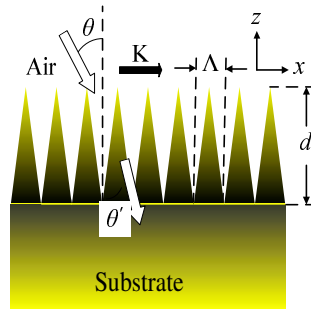


Fig. 5. The schematic diagram of a BAM arrays

### 3.1 Fourier model method

The transmittance performance and near-field distribution of the BAM were performed by a rigorous vector method of Fourier model method (FMM). The FMM derived from the exact solution of Maxwell's equation has been commonly applied to yield accurate diffraction characteristic and near-field distribution regardless of the feature size of surface structure [21,22]. Then, the reflection and transmission coefficient matrix propagation algorithm (RTCM) [23], a numerically more efficient variant of  $S$ -matrix algorithm than any of known form [24], is used to calculate the amplitude coefficient matrix of modal fields with the boundary conditions.

Moreover, it is well known that the accuracy of FMM is dependent on the number of spatial harmonics used to represent the periodic electromagnetic field, and the calculated results converge to the exact solution as the number of spatial harmonics is increased. Hence, a sufficient number of harmonics in addition to the adequate divided multilayer lamellar grating for the surface structure were retained in all our calculations to ensure accuracy.

### 3.2 Broadband transmittance characteristic

Figure 6 shows plots of the zero order transmittance calculated by the rigorous FMM with respect to the groove depth and periodicity of the BAM with the both incident wavelengths of 1064nm and 532nm for TE and TM polarization, respectively, at normal incidence. The white region of transmittance for (a), (b), (c) and (d), respectively, in Fig. 6 exhibits the transmittivity  $\geq 99.8\%$ . On the basis of the higher diffraction efficiency of the microstructure arrays in Fig. 6, the broadband antireflective property to the BAM for both TE and TM polarization at normal incidence is shown in Fig. 7 with the variation of groove depth and period, respectively. The sharply drop of the transmittance demonstrated in Fig. 7 can be explained resulting from the appearance of higher diffraction orders.

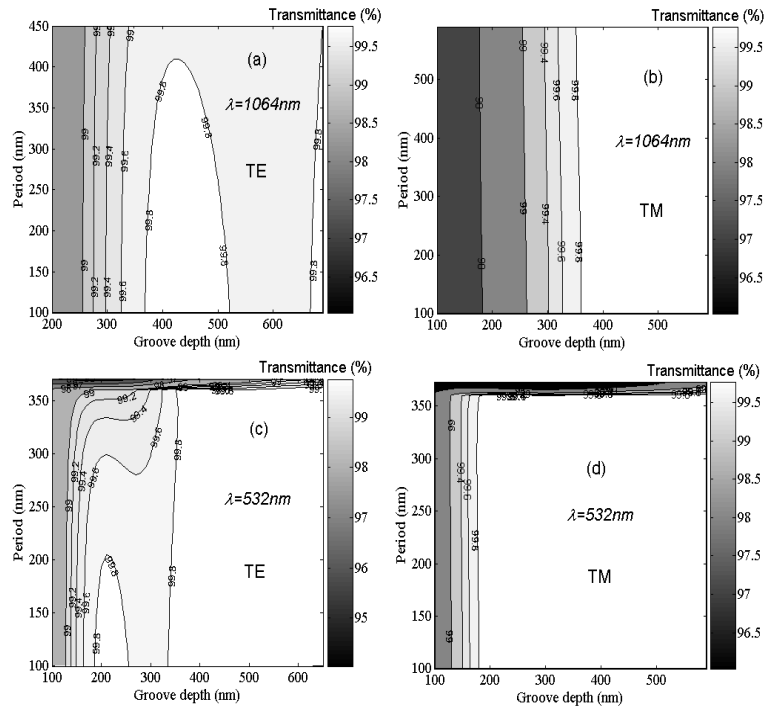


Fig. 6. Parameter scan of transmittance as a function of the groove depth and period for the BAM arrays at normal incidence. (a) and (c) exhibit the incident wavelength of 1064nm and 532nm, respectively, for TE polarization. (b) and (d) indicate the incident wavelength of 1064nm and 532nm, respectively, for TM polarization.

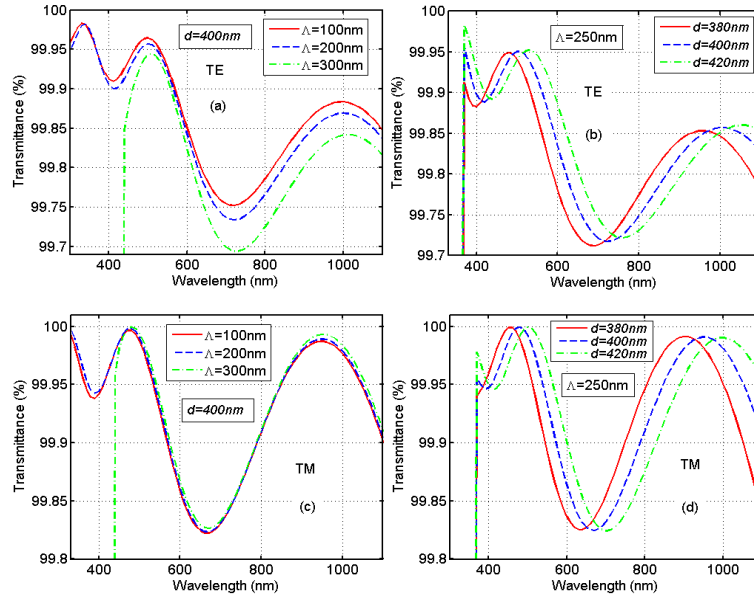


Fig. 7. The zero order transmission efficiencies as a function of the incident wavelength at normal incidence with the variation of the groove depth and the period, respectively. (a) and (b) for TE polarization. (c) and (d) for TM polarization.

### 3.3 Near-field distribution

Based on diffraction efficiency  $\geq 99.8\%$  calculated in Fig. 6, the near-field distributions of the BAM as a function of the surface structure period with the groove depth of 400nm for both TE and TM polarizations are simulated numerically by the FMM for the incident wavelength of 1064nm and 532 nm shown in Fig. 8 and Fig. 9, respectively, at normal incidence. Besides, the factor  $q$  of the quantitative electric field enhancement, which  $q = |E_t / E_i|$  is defined as the ratio of the internal field  $E_t$  in microstructure to the incident field  $E_i$ , is shown in near-field distribution images. In both the Fig. 8 and Fig. 9, we can see that the near-field distribution is strongly dependent on the periodicity of surface structure for TE wave. But, for TM polarization the near-field distribution is insensitive to the period of surface profile, and the strong electric field region is distinctly distributed in the groove of surface microstructure, which is potential to promote the ability of anti-laser-induced damage. Furthermore, it is evident that the enhancement of electric field with the incident wavelength of 1064nm shown in Fig. 8 is larger than that of the incident wavelength of 532nm shown in Fig. 9 with the same surface parameters for TE polarization, but for TM wave the enhancement factor  $q=1.0$  is revealed on the top of the ridge of BAM for the both wavelengths no matter what the surface parameters are.

In addition, it is worth mentioned that the variation of the near-field distribution as a function of the groove depth with a fixed period of surface structure is slight for the both TE and TM polarizations regardless of the incident wavelength.

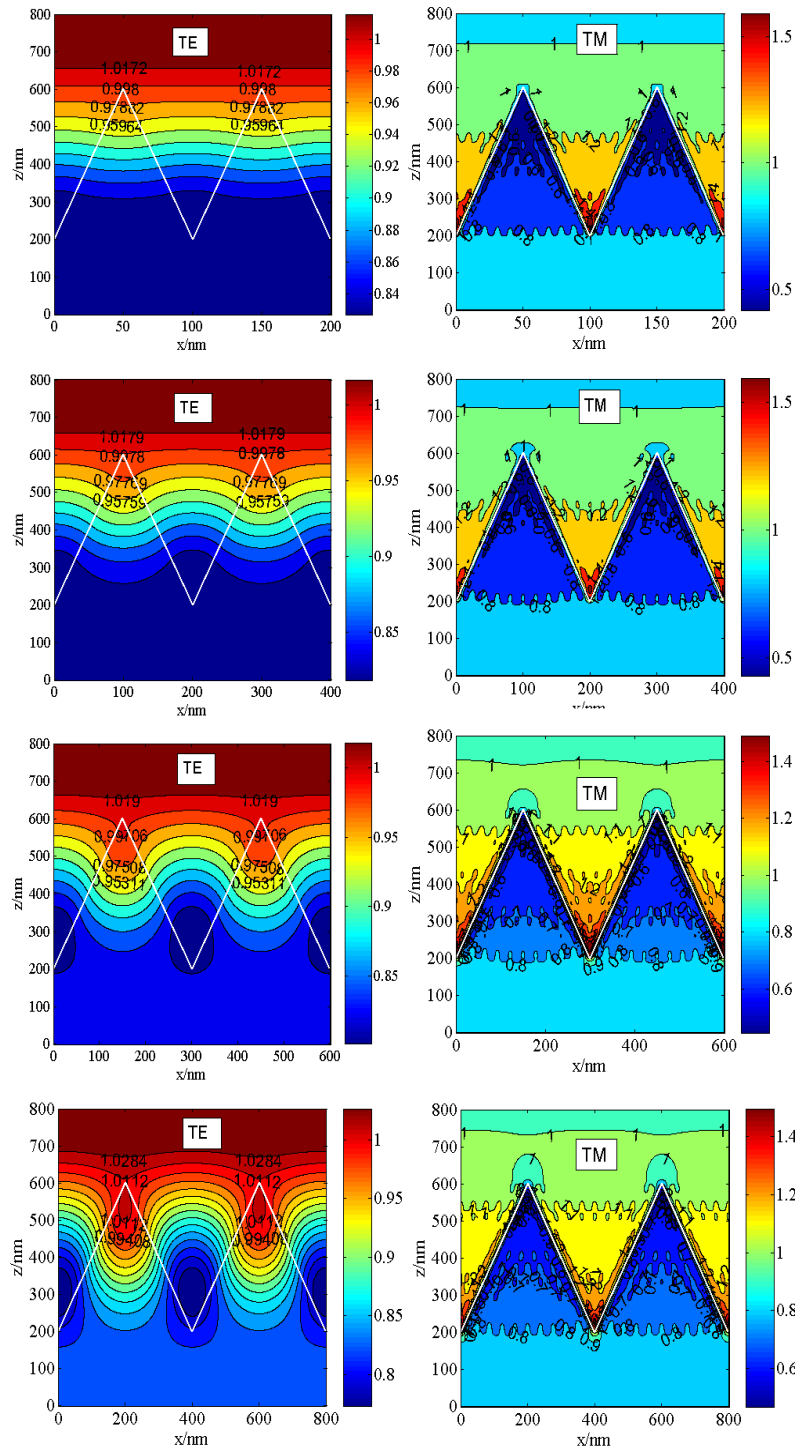


Fig. 8. The normalized near-field distribution calculated quantitatively by the FMM for both TE and TM polarizations. The periods of 100nm, 200nm, 300nm and 400nm, respectively, with the groove depth of 400nm for the incident wavelength of 1064nm at normal incidence on the basis of the transmittance  $> 99.8\%$  are performed in sequence.

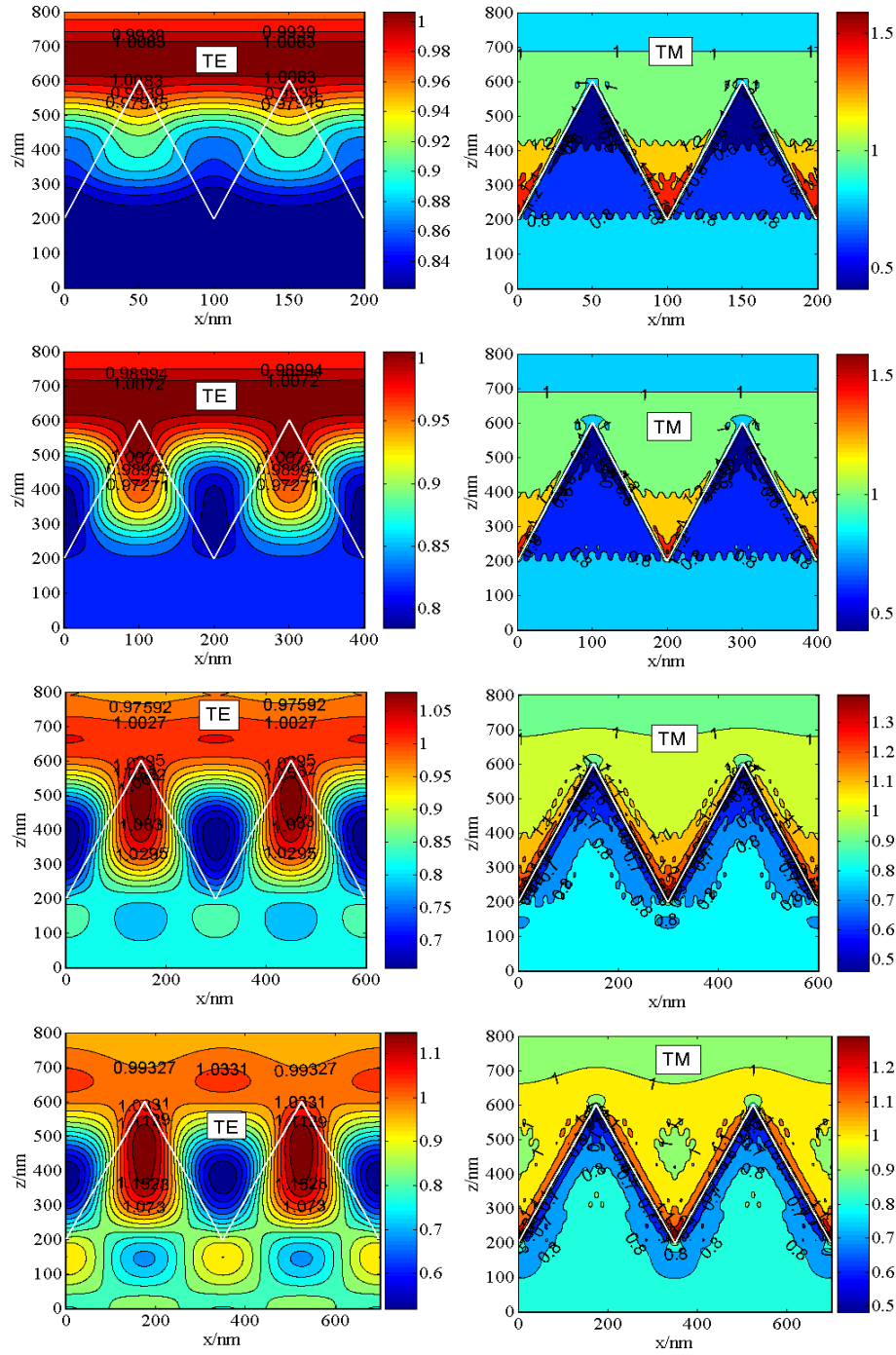


Fig. 9. The normalized near-field distribution with the same parameters of Fig. 8 except for the incident wavelength 532nm. The periods of 100nm, 200nm, 300nm and 350nm, respectively are performed in sequence.

#### 4. Femtosecond damage threshold as a function of pulse duration

According to the quantitatively calculated near-field distribution shown in Fig. 8 and Fig. 9 for the incident wavelength of 1064 and 532nm, respectively, at normal incidence, the single-shot ultra-short pulse damage threshold taking account of the maximum electric field enhancement factor  $q$  in the BAM with the substrate band gap  $E_g = 9\text{eV}$  was predicted by the rate equation of Eq. (2) using the CED as the damage criterion. And the original zero electron density in the CB was assumed to calculate electrons excitation.

Figure 10(a), 10(c) indicates the changing characteristic of both the maximum electric field enhancement in the BAM and the corresponding damage threshold predicted as a function of the surface structure period for the pulse duration 100fs. For the incident wavelength 1064nm shown in Fig. 10(a), it can be seen that the maximum enhancement shown in lower region of the image increases gradually as the surface periodicity increases for TE polarization, but for TM wave the value of  $q$  is unchanged basically with respect to the surface period. And the calculated damage threshold corresponding to the maximum electric field enhancement as a function of the surface structure period is shown in the top range of the image, it can be obtained that the damage threshold decreases gradually as the period increases for TE wave. But for TM polarization the LIDT is unchanged on the surface periodicity. For the incident wavelength of 532nm shown in Fig. 10(c), the varying feature of both the maximum electric field enhancement and the corresponding LIDT as a function of the surface period is similar to that of the incident wavelength 1064nm.

Figure 10(b), 10(d) shows the damage threshold fluence of the BAM as a function of pulse duration for both TE and TM polarizations with the incident wavelengths of 1064nm and 532nm, respectively, shown in Fig. 10(b) and Fig. 10(d). In addition, multiple pulse accumulation effects are known to lower the breakdown threshold of materials. And the functional dependence of the threshold fluence on the pulse duration for the single and multiple pulse case and the principal damage mechanisms are very similar. Several groups have reported recently that, due to incubation effects, the threshold for multiple-shot experiments is lower than that for single-shot experiments by a factor of approximately two for ultra-short laser pulses [25].

Figure 10(b) shows the LIDT with respect to the pulse duration allowing for the maximum factor  $q$  for both TE and TM polarizations with the incident wavelength of 1064nm. It can be seen that the weak linear dependence of the threshold fluence on the femtosecond pulse width is shown, and the influence of the periodicity corresponding the different maximum electric field enhancement factor  $q$  to the LIDT is slight for TE and TM polarization. In other words, the ability of anti-laser-induced damage of the BAM is nearly independent on the periodicity of surface structure for longer incident wavelengths. Besides, the weakly linear breakdown thresholds on the pulse duration are in agreement well with the experimental measurements of Stuart *et al*, Lenzner *et al* and Tien *et al* [4].

However, for the incident wavelength of 532nm the breakdown threshold as a function of pulse duration shown in Fig. 10(d) shows an evident oscillation peak, which is similar to the measurement result of Du *et al* [26]. Moreover, the effect of the surface periodicity associated with the field enhancement factor  $q$  is visible larger, and the damage threshold decreases as the period of surface structure increases. Accordingly, for the shorter incident wavelengths the damage property of the BAM is sensitive to surface period for TE polarization, but for TM polarization the damage threshold is almost independent on the periodicity on the basis of the near-field distribution of Fig. 9.

The dependence of damage threshold on wavelength can be due to the frequency-dependent PI rate. For the MPI, shorter wavelengths with the larger photon energy have higher electron yields than longer wavelengths. When the electric field is extremely high, TI should be considered instead of MPI. In the tunnel-ionization regime, the electric field of the laser suppresses the Coulomb well which binds a valence electron to its parent atom so that the bound electron tunnels through the short barrier and becomes free, then the dependence of

damage threshold on wavelength becomes weak. But, for the produced electrons dominated by AI in the CB, since the momentum relaxation time in solids is less than a femtosecond, which is shorter than an optical cycle in the visible range, the ED is nearly independent of the wavelength. Therefore, the damage threshold for longer wavelengths with a fixed pulse duration is rational larger than that for shorter wavelengths in the MPI region. However, the LIDT for shorter wavelength of 532nm shown in Fig. 10(d) demonstrates a surprising oscillation peak. To this phenomenon, Tien *et al.* developed a theoretical model combining the Keldysh's PI and the AI model of Thornber, with which the oscillation of the LIDT on the pulse duration can be explained on the basis of the different initial free ED in the CB [4]. Nevertheless, the calculated LIDT with their theoretical model is largely low in contrast with experimental measurements. Furthermore, according to our proposed theoretical model with the initial zero ED in the CB, the LIDT exhibiting an oscillating peak on the pulse duration for the shorter incident wavelength is in agreement reasonable with the experimental result.

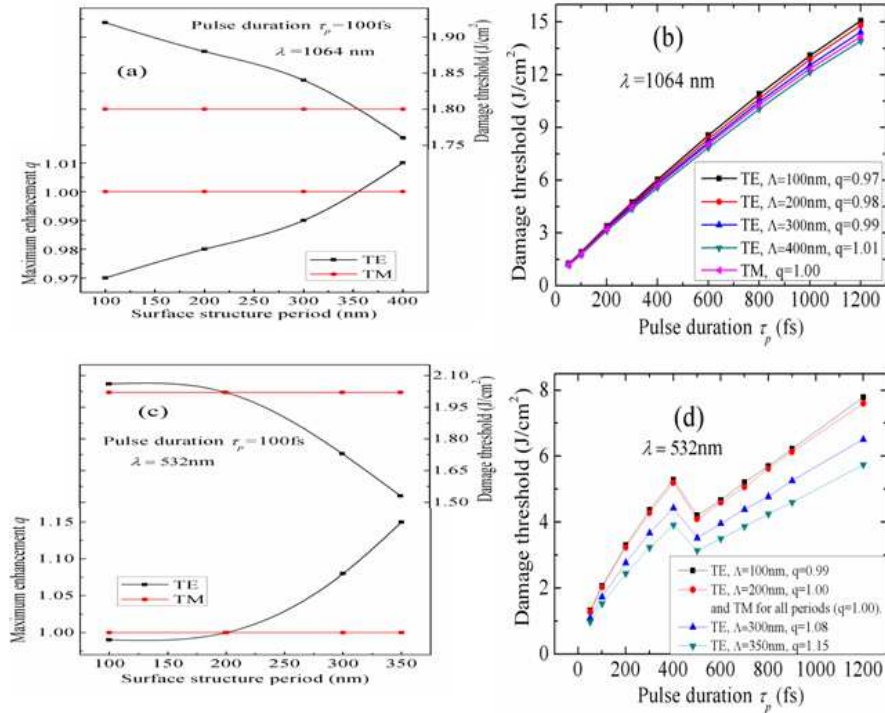


Fig. 10. (a)(c) The varying characteristic of both the local maximum electric field enhancement  $q$  and the corresponding damage threshold as a function of the surface structure period based on the Fig. 8 and Fig. 9 for the laser pulse duration 100fs. (a) for the incident wavelength of 1064nm, (c) for the incident wavelength of 532nm. (b)(d) The calculated damage threshold as a function of the pulse duration taking account of the local maximum electric field enhancement  $q$  in the Fig. 8 and Fig. 9, respectively. (b) for the incident wavelength of 1064nm. (d) for the incident wavelength of 532nm.

Moreover, it is currently known that the optical coatings are commonly applied to high-power laser systems for the antireflective components. In order to suppress reflection in a large range of wavelengths, a multilayer dielectric antireflection coatings, consisting of alternating thin layers of high and low refractive index, designed finely by utilizing thin-film interference principle requires a mass of film layers which inevitably increase the potential for unacceptable laser damage levels. Although Jasapara *et al.* [5] and Mero *et al.* [6] indicated that in femtosecond pulse breakdown range the damage behavior of high-quality thin films is similar to bulk materials and defects and impurities play a negligible role, the LIDT of a multilayer coating is often dominated by the high refractive index material, possessing smaller band gap, which is easy to be ionized with the strong laser radiation. Thus the LIDT of a



broadband antireflective multilayer coating is generally smaller than that of the BAM arrays directly built in the substrate material having hard ionized larger band gap. Therefore, it is expected that the BAM with smaller period instead of optical coatings can be applied to high-power laser systems as a laser-transmitting optical element requiring high LIDT.

## 5. Summary

A theoretical model combining the Keldysh's PI with Drude's AI in addition to the ED decay term was proposed for more precisely estimating the ultra-short pulse LIDT. Then, the near-field distribution in the 'moth eye' structure performed by the FMM exhibits a strongly dependence on the surface period for TE polarization, but for TM wave it is insensitive to the periodicity of the surface profile. Moreover, the femtosecond LIDT of the BAM on the pulse duration taking the local electric field enhancement into account displays a weak linear relationship for the incident wavelength of 1064nm, while a surprising oscillation peak appears for the wavelength of 532nm. What's more, it is expected that the broadband antireflective 'moth eye' surface microstructure directly built into the substrate material associated with the promising higher LIDT can be applied to high-power laser systems as a transmitting optical component.

## Acknowledgments

This work is supported by the National Natural Science Foundation of China (Grant No.10704079).